Proceedings of the ASME 2012 10th International Conference on Nanochannels, Microchannels, and Minichannels
ICNMM2012
July 8-12, 2012, Rio Grande, Puerto Rico

ICNMM2012-73

FLUID FLOW AND HEAT TRANSFER SIMULATIONS OF THE COOLING-WATER CHANNEL IN A TERA-HERTZ RADIATION DETECTOR

Usama Tohid, Arturo Pacheco-Vega*
Department of Mechanical Engineering
California State University–Los Angeles
Los Angeles, CA 90032, USA
E-mail: apacheco@calstatela.edu

Rodion Tikhoplav, Marcos Ruelas
RadiaBeam Technologies LLC
1717 Stewart St.
Santa Monica, CA 90404, USA

ABSTRACT

Detailed numerical simulations have been carried out to find the velocity and temperature fields of a rectangular channel with large aspect-ratio. The channel under analysis is aimed to cool a thermo-chromic liquid crystal material (TLC) that is able to capture laser irradiation in the terahertz range. The overall objective of the cooling system is to maintain a nearly-homogeneous temperature of the TLC layer that is not exposed to the direct laser irradiation. The fluid flow and heat transfer simulations are carried out on the basis of three-dimensional versions of the Navier-Stokes equations, along with the energy equation, for an incompressible flow, to determine values of velocity, pressure and temperature inside the channel under different operating conditions. These values are then used to find, from a specific set, the value of the channel height that allows for the most uniform temperature distribution within the expected operating conditions. Results from this analysis indicate that, for all the inlet velocities considered, there is a common value of the channel height, that represents the optimum.

NOMENCLATURE

A surface area
c specific heat of fluid
h heat transfer coefficient
k thermal conductivity of fluid
L channel length
p pressure
q_{in} heat rate
q''_{in} heat flux
T fluid temperature
T_w^{in} inlet fluid temperature
T_∞ ambient temperature
$\mathbf{u}$ Cartesian velocity vector
u_{in} inlet velocity
W channel width
x, y, z Cartesian coordinates

Greek symbols
Δp pressure drop
ΔT_m maximum temperature difference
δ channel gap (height)
∇ Nabla operator
ν kinematic viscosity
ρ fluid density

Subscripts and superscripts
max maximum
min minimum
opt optimum

INTRODUCTION

During the last decade there has been tremendous progress in the field of Terahertz (THz) science. The previously unex-

*Address all correspondence to this author.

ploited "THz gap" of the electromagnetic spectrum, which includes far infrared (FIR) and sub-millimeter waves, was actively explored through developments of new sources, detectors and technologies [1,2]. The possibility of practical applications of THz radiation became apparent in many areas ranging from far-infrared astronomy, and time-resolved THz spectroscopy [3] to skin cancer diagnostics [4] and other medical applications as well as detection of explosives and biohazards. With the development of high power synchrotron sources spanning over a wide range of wavelengths, as well as tunable FIR free-electron lasers [5], the need for large aperture THz detector becomes apparent [6].

The THz imaging device described here (T-camera^{TM}), based on thermo-chromic liquid crystal (TLC) as a sensitive element, has a potential to become an important tool to cover the sub-millimeter range of the radiation spectrum. However, because of the high-sensitivity of the TLC-layer, it is fundamental to maintain its background temperature as homogeneous as possible to minimize spurious readings. Thus, the objective of the present work is to determine the channel height; i.e., the gap of a cooling water channel necessary to maintain a nearly-homogeneous reference temperature of the TLC layer of a THz-radiation detector. To this end, detailed three-dimensional numerical simulations are carried out to determine the velocity and temperature fields in the rectangular channel. The numerical runs are carried out in a parametric way for a set of channel-height values and different operating conditions to determine the channel-gap that allows for the most uniform temperature distribution within the expected experimental conditions. The results are presented in terms of pressure drops, temperature distributions and maximum temperature differences within the channel as functions of the channel height and inlet cooling-water velocities.

1 PROBLEM DESCRIPTION

A thorough description of the THz-detection system considered here, along with its characteristics, can be found in c.f. [7], and only a brief account is provided next. The principle of operation of T-camera is based on the property of the thermochromic liquid crystal (TLC) to change its color when heated: the molecular structure of TLC changes with temperature, producing a change in the optical properties of the material. Hence, by imaging the TLC surface with a color video camera, one can determine the temperature map of the surface.

The T-camera specifications and its schematic are presented in Table 1 and in Fig. 1(a), respectively. Since the TLC response is purely thermal, there is no fundamental limitation on the wavelength range to which the T-camera is sensitive, and the very same device can be used to image radiation beams in a very broad spectral range, depending only on the limits of the absorber attached to the TLC sheet.

In reference to Fig. 1(a), the incoming radiation beam is delivered towards the sensitive layer, which is a thin absorptive material on which a TLC sheet is attached. The other side of the sensitive layer is attached to a thermally-stabilized transparent water chamber that allows for back-view geometry. A computer controlled system is used to maintain the inlet temperature of the cooling water within the range where a particular TLC material exhibits the strongest optical response to a minimal change in temperature. Proper thermal analysis is of paramount importance for effective design of the cooling system and is done numerically as described below.

Table 1. T-CAMERA SPECIFICATIONS.

Parameter	*Value*
Wavelength operational range	1 μm – 200 μm
Spatial resolution	250 μm; 200 $\times$ 160, 32 kpix
Sensitivity	100 μJ/cm^2
Active area	50 mm $\times$ 40 mm, 20 cm^2

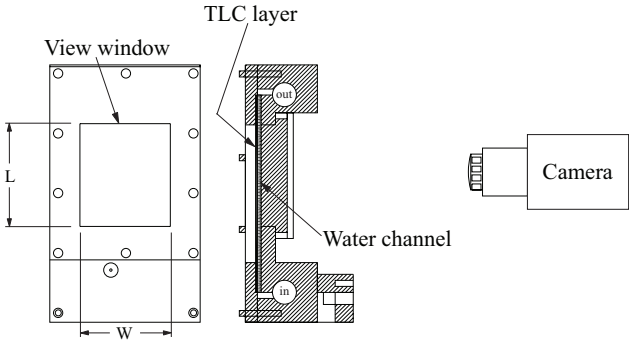

(a) SCHEMATIC.

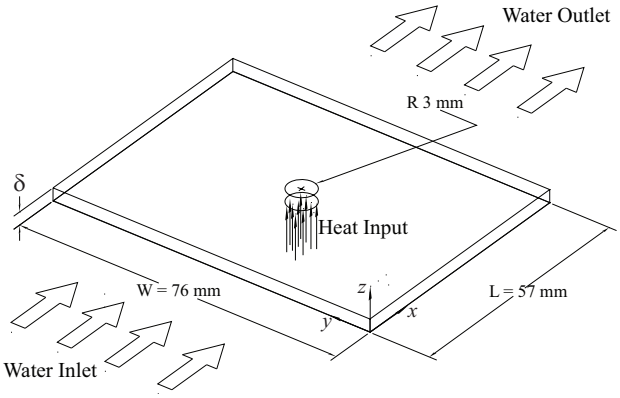

(b) COMPUTATIONAL DOMAIN.

Figure 1. THZ IMAGING DETECTOR SYSTEM.

2 GOVERNING EQUATIONS

A schematic of the section of the water channel considered for the numerical simulations is shown in Fig. 1(b). The dimensions are given by the channel length $L = 57$ mm (x-direction), its width $W = 76$ mm (y-direction), and a variable channel gap δ (z-direction). The fluid flow is in the x-direction. Neglecting body forces and viscous dissipation, the continuity, momentum and energy equations for an incompressible, Newtonian fluid with constant properties, in the laminar regime and under steady-state conditions, can be written in vector form as

$$\nabla \cdot \mathbf{u} = 0, \tag{1}$$

$$(\mathbf{u} \cdot \nabla)\mathbf{u} = -\frac{1}{\rho}\nabla p + \nu \nabla^2 \mathbf{u}, \tag{2}$$

$$\rho c (\mathbf{u} \cdot \nabla) T = k \nabla^2 T, \tag{3}$$

where $\mathbf{u}$ is the three-dimensional Cartesian velocity vector with components u, v and w, in the directions x, y and z, respectively; p is the pressure, ρ the fluid density, c the specific heat, k its thermal conductivity and T is the water temperature.

For the fluid flowing inside the channel, the boundary settings are the typical no-slip and impermeable conditions at the solid walls; a uniform influx velocity condition u_{in} is enforced at the inlet cross section, and zero pressure with no viscous stresses are set at the outlet. In reference to Fig. 1(b), the thermal boundary conditions are as follows: the fluid enters the channel with a uniform temperature T_w^{in} (as provided by a PID controller), and leaves it under the assumption of periodic conditions. At the plane $z = 0$, where the channel is in contact with the acrylic plate –and along the side walls– the condition set is thermal insulation. On the other hand, at the plane $z = \delta$, the heat transfer between the water in the channel and the ambient air at T_∞ is by convection, the exception being the circular region at the center of the wall which receives electromagnetic irradiation at a rate q''_{in}. It is to note that the thermal resistance to conduction across the TLC layer has been neglected due to its exceedingly-small thickness.

3 NUMERICAL SOLUTION

The governing equations were discretized on the domain and solved by the well-known finite element method. COMSOL Multiphysics[1] software is used for this purpose. Given a channel geometry, i.e., a value of δ, a three-dimensional unstructured mesh is built using four-node tetrahedral elements with quadratic Lagrange interpolating functions for both the temperature and the velocity components, and linear Lagrange polynomials for the pressure. In this type of element, both temperature and velocity degrees of freedom are assigned at each node and each edge of the element, whereas the pressure degree of freedom is associated only with the nodes. The velocity and temperature fields are obtained by computing the system of algebraic equations simultaneously via the biconjugate gradient stabilized (BiCGStab) iterative solver. The relative tolerance was set to 10^{-6}. To ensure grid independence of the corresponding results, several grids were tested for different values of the inlet velocity and channel gap, including their lower and upper bounds. Figure 2 illustrates a typical set of convergence tests for the pressure drop in the streamwise direction, for three values of the channel gap and two different inlet velocities. From the figure it can be seen that, regardless of the inlet velocity and channel gap, a grid with 8500 elements is sufficient to achieve an accuracy within 2% of the results obtained with a grid containing twice a many elements in each direction.

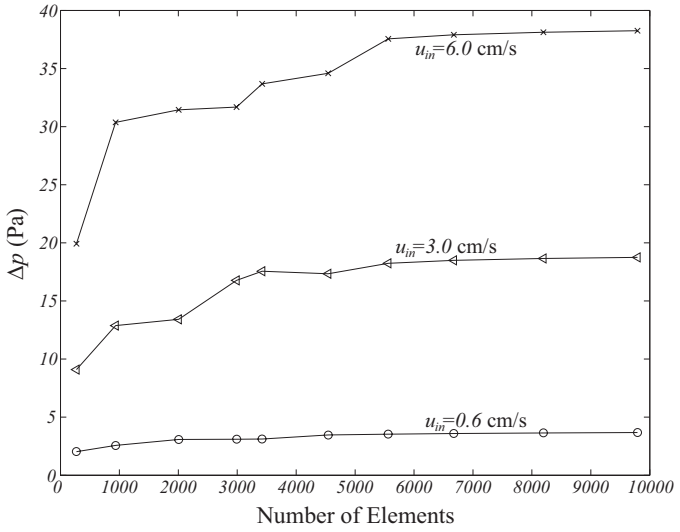

Figure 2. GRID INDEPENDENCE TESTS FOR $\delta = 1$ mm AND THREE INLET VELOCITIES.

4 RESULTS AND DISCUSSION

The goal of the numerical study is to find the optimum channel gap, δ_{opt}, that maintains a homogeneous reference temperature for the TLC layer. The mathematical model was solved for different geometries (i.e., the channel gap δ), and different sets of operating parameters (i.e., $\{u_{in}, q''_{in}, T_\infty, T_w^{in}\}$). Their ranges are: $\delta \in [1,6]$ mm in intervals of 1 mm, $u_{in} \in [0.6,6]$ cm/s, divided in five values that are directly related to the volumetric flow rate of the pump, an energy influx $q_{in} \in [0.001, 0.5]$ W over a variable circular area of $A \in [0.031, 3.1]$ cm^2, which correspond to an electromagnetic irradiation of $q''_{in} = 318$ W/m^2 for the small-

[1] http://www.comsol.com

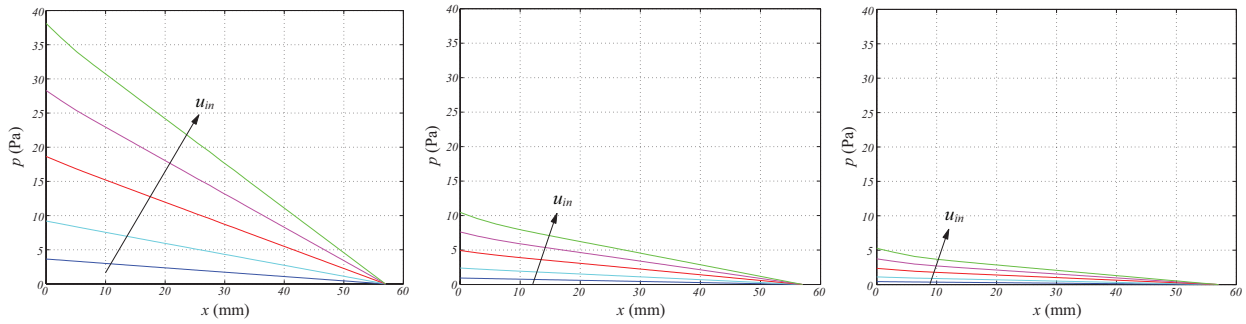

(a) $\delta = 1$ mm (b) $\delta = 2$ mm (c) $\delta = 3$ mm

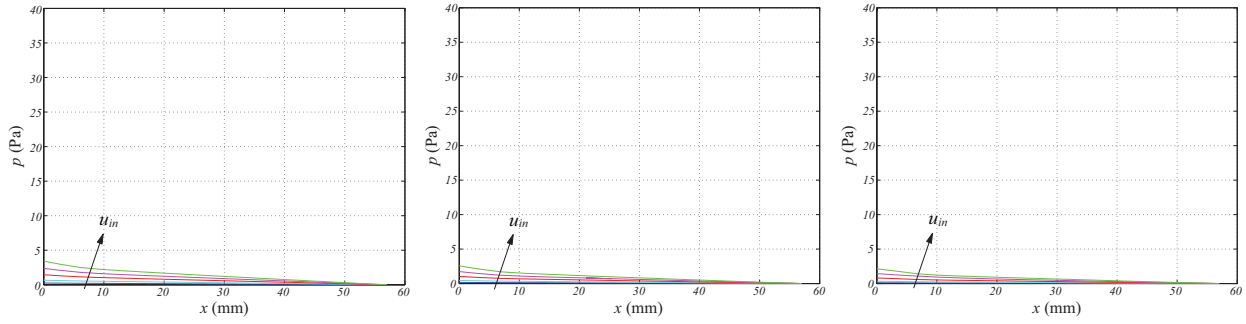

(d) $\delta = 4$ mm (e) $\delta = 5$ mm (f) $\delta = 6$ mm

Figure 3. PRESSURE DROP ALONG THE CHANNEL FOR SEVERAL INLET VELOCITIES. ARROWS INDICATE DIRECTION OF INCREASING VELOCITY.

est heat input and 1593 W/m^2 for the highest, $T_\infty \in [20,30]^\circ$C, and $T_w^{in} \in [25,35]^\circ$C, both in intervals of 5°C. The physical properties for the fluid are: $\nu = 1.125 \times 10^{-6}$ m^2/s, $\rho = 1000$ kg/m^3, $c = 4.18$ kW/kg K and $k = 0.61$ W/m K, whereas the heat transfer coefficient considered was $h = 20$ W/m^2 K, which is a typical value for a condition of natural convection heat exchange with the environment.

Typical pressure distributions along the channel streamwise direction are shown in Fig. 3 for the five velocities; i.e., $u_{in} = \{0.6, 1.5, 3.0, 4.5, 6.0\}$ cm/s, and the six channel gaps considered. From the set of figures 3(a)–3(f) it can be seen that, regardless of the gap size δ, as expected, the pressure drop along the channel, Δp, increases with increasing inlet velocity of the water flowing into the channel, as driving a larger mass flow rate requires a larger pressure force. Also expected is the fact that this behavior is more pronounced at smaller gap sizes; i.e., $\delta = 1$ mm, for which the friction coefficient is substantially higher than that for larger channel gaps. As can be seen, for example, the value of Δp for $\delta = 3$ mm is bounded at 13% of that for $\delta = 1$ mm and at 50% of that for $\delta = 2$ mm.

The results from the heat transfer analysis are shown in Figs. 4 and 5, in terms of temperature distributions and profiles at different sections of the channel. Though this results are for a heat influx $q''_{in} = 318$ W/m^2, an ambient temperature $T_\infty = 20^\circ$C (293.15 K), and an inlet water temperature $T_w^{in} = 25^\circ$C (298.15 K), results corresponding to the other thermal conditions are qualitatively similar.

The temperature distributions of Figs. 4(a)–4(c) at planes $z = 0$, $\delta/2$, and δ, respectively (for $\delta = 1$ mm and $u_{in} = 0.6$ cm/s) show some degree of stratification with regions of high-, medium-, and low-temperature values resulting from the uniformity of the velocity field and the regular exchange of energy with the environment. At the center section of each plane, however, the effect of the heat input can be readily noticed as the temperature distribution around and above the circular heated area resembles that of a plum due to the energy being advected towards the channel outlet. As expected, this advection-diffusion effect is more pronounced at the plane in contact with the TLC layer ($z = 0$) being a result of the higher energy exchange, becoming negligible at the top surface ($z = \delta$), as seen in Fig.4(d).

The set of Figs. 5(a)–5(f) illustrates typical temperature profiles along the centerline of the channel in the streamwise direction, for the set of five inlet velocities and six channel gaps considered. From the figures two main features can be observed. The first is that, regardless of the gap size, at small inlet velocities the temperature profiles change substantially whereas at higher velocities (i.e., larger flow rates) the temperature profiles are essentially uniform. This is expected since the residence time of

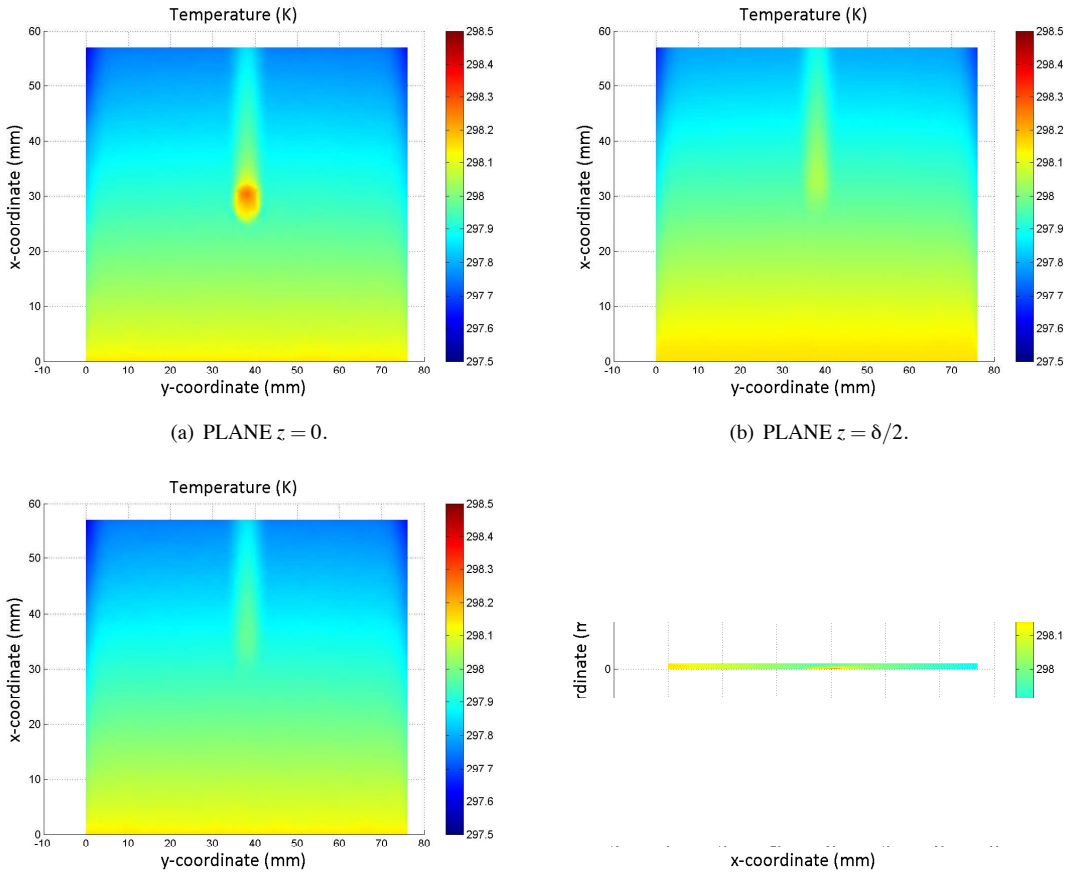

(a) PLANE $z = 0$.

(b) PLANE $z = \delta/2$.

(c) PLANE $z = \delta$.

(d) PLANE $x = W/2$.

Figure 4. TEMPERATURE DISTRIBUTION AT DIFFERENT PLANES FOR $\delta = 1$ mm.

the water exchanging energy with both the ambient in the first – and last– 25 mm along the x-coordinate, and the laser irradiation within the 10 mm diameter at the center of it, is larger at small velocities. The second characteristic is that, as the gap size increases, the influence of the inlet velocity upon the temperature profile decreases substantially, hence decreasing the temperature difference between its maximum and minimum values which, depending on the gap size, occur at different locations along the centerline.

It should be pointed out that although higher velocities provide smaller temperature differences, they also imply larger mass flow rates and hence larger local stresses upon the TLC layer, which in the end may cause its deformation and consequently appreciable measurement errors. Furthermore, it is also important to note that temperature profiles in the channel change both qualitatively and quantitatively with operating conditions (particularly the influx of energy from the laser beam), and that maximum and minimum temperature values may occur at points within the domain different from those considered previously along the centerline. Thus, since the objective is to maintain a homogeneous background temperature for the TLC layer, then it is important to seek the gap size that minimizes this temperature difference; i.e., $\Delta T_m = T_{max}(x,y,z) - T_{min}(x,y,z)$.

The result from an exhaustive search to find the optimum gap size, δ_{opt}, is shown in Fig. 6. The figure illustrates the distribution of ΔT_m values as functions of the gap size and inlet velocity for $u_{in} = \{0.6, 1.5, 3.0, 4.5, 6.0\}$ cm/s. From the figure it is clearly seen that, as expected, regardless of the value of δ, smaller inlet velocities provide larger values of ΔT_m due to the larger residence times. However, more important is the fact that for all the fluid velocities considered, there is one single gap size ($\delta = \delta_{opt} = 3$ mm) for which ΔT_m achieves the minimum value. Although for the operating conditions reported here (i.e., $q''_{in} = 318$ W/m^2 with $q_{in} = 0.01$ W) $\delta_{opt} = 3$ mm, for smaller values of the heat input q_{in} (while maintaining all other conditions unaltered), the optimum value of δ was found to decrease. On the other hand, for the largest heat input considered in this project –$q_{in} = 0.5$ W– there is not a definitive optimum value for

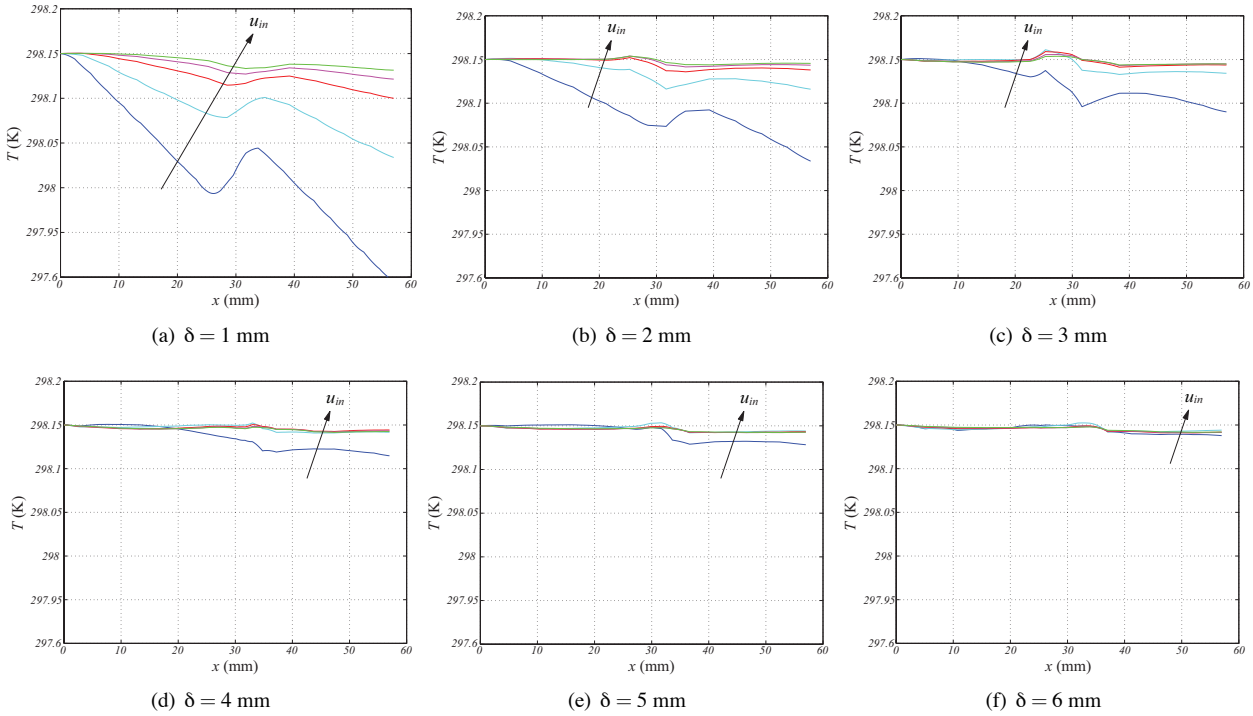

(a) $\delta = 1$ mm (b) $\delta = 2$ mm (c) $\delta = 3$ mm

(d) $\delta = 4$ mm (e) $\delta = 5$ mm (f) $\delta = 6$ mm

Figure 5. TEMPERATURE PROFILES ALONG THE CHANNEL CENTERLINE FOR FIVE DIFFERENT INLET VELOCITIES. ARROWS INDICATE DIRECTION OF INCREASING VELOCITY.

the gap size located within the design domain. Experimental results, reported elsewhere [8], have shown that the optimum value found in this study provides a substantially better accuracy in the measurements from the THz imaging device.

5 CONCLUDING REMARKS

Parametric analyses, via numerical simulations, provide an advantageous approach for obtaining accurate solutions of complex engineering systems, which otherwise would be extremely difficult to obtain experimentally under reasonable allocation of time and resources. In this investigation we have found, through a parametric analysis, the optimum solution for the channel gap that provides a nearly-homogeneous temperature reference for the TLC layer in a THz imaging device. For a given heat influx originated from a laser source, the numerical simulations indicate that there is a common value of the channel gap (height) of the cooling system, that represents the optimum for all the inlet velocities within the range considered.

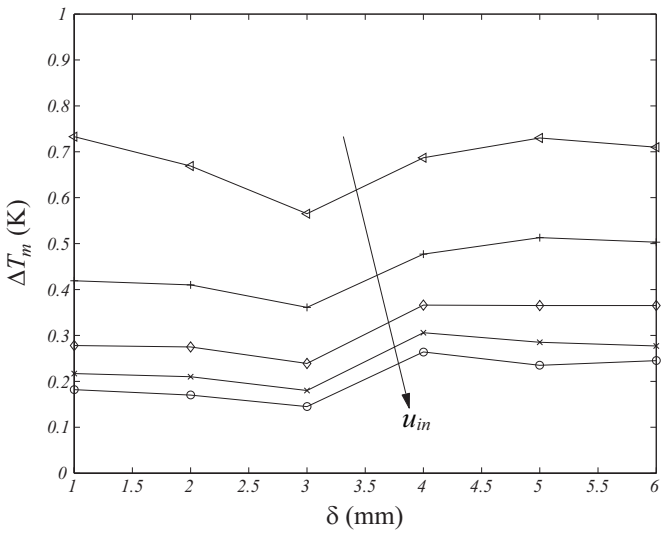

Figure 6. ΔT_m VS. δ FOR DIFFERENT INLET VELOCITIES. ARROW INDICATES DIRECTION OF INCREASING VELOCITY.

ACKNOWLEDGMENT

U. Tohid is the recipient of a CEaS fellowship for which we are grateful. This work has been supported by NSF IIP-0724505 and HRD-0932421 grants.

REFERENCES

[1] Borak, A., 2005. "Toward bridging the terahertz gap with silicon-based lasers". *Science*, **308**(5722), pp. 638–639.

[2] Ferguson, B., and Zhang, X.-C., 2002. "Materials for ter-

ahertz science and technology". *Nature Materials,* **1**(1), pp. 26–33.

[3] Schmuttenmaer, C., 2004. "Exploring dynamics in the far-infrared with terahertz spectroscopy". *Chemical Reviews,* **104**(4), pp. 1759–1779.

[4] Woodward, R., Cole, B., Wallace, V., Pye, R., Arnone, D., Linfield, E., and Pepper, M., 2002. "Terahertz pulse imaging in reflection geometry of human skin cancer and skin tissue". *Physics in Medicine and Biology,* **47**(21), pp. 3853–3863.

[5] Carr, G., Martin, M., McKinney, W., Jordan, K., Neil, G., and Williams, G., 2002. "High-power terahertz radiation from relativistic electrons". *Nature,* **420**(6912), pp. 153–156.

[6] Shaftan, T., and Yu, L., 2005. "High-gain harmonic generation free-electron laser with variable wavelength". *Phys. Rev. E,* **71**(4), p. 046501.

[7] Tikhoplav, R., Andonian, G., Pacheco-Vega, A., Ruelas, M., Shaftan, T., and Sharif, A., 2011. "Status on the development of the terahertz camera". In Proceedings of the 36th International Conference on Infrared, Millimeter, and Terahertz Waves, pp. 1–2. IRMMW-THz-1733887.

[8] Pacheco-Vega, A., Tikhoplav, R., Tohid, U., Ruelas, M., and Sharif, A., 2011. Cooling system optimization for a terahertz radiation detector via thermal parametric analysis. Submitted to *Applied Thermal Engineering*.